Journal of Marine Research, 69, 435–461, 2011

Ellipsoidal vortex in a nonuniform flow: Dynamics and chaotic advections

by V. V. Zhmur[1,2] E. A. Ryzhov[3] and K. V. Koshel[3,4,5,6]

ABSTRACT

Quasi-geostrophic dynamics of an ellipsoidal vortex embedded in a nonuniform flow is studied in the approximation of the infinitely deep rotating ocean with a constant buoyancy frequency. The vortex core is an ellipsoid with a constant vorticity different from the background vorticity value. The core is shown to move along with the flow and to deform under the effect of it. Regimes of the core's behavior depend on the flow characteristics and the initial values of the vortex parameters (the shape and the orientation relative to the flow). These regimes are (i) rotation (along with the eccentricity oscillation), (ii) oscillation about one of the two specific directions (along with the eccentricity oscillation), and (iii) infinite horizontal elongation of the core. The localized regimes (rotation and oscillation) of the core motion are analyzed. It is shown, that zones of the water mass capturing can appear in the induced velocity field. The mechanisms of fluid particle trajectory chaotization are revealed; in particular, it is shown that, owing to the double periodicity of the core motion, all the nonlinear resonances appear as pairs of two resonance islands with the same winding number.

1. Introduction

Synoptic and mesoscale oceanic structures have horizontal velocities U of the order of 0.1–1 m/s, characteristic horizontal scales L of the order of 10–100 km, and vertical velocities three or four orders less than the horizontal ones. According to the classification by Ivanov *et al.* (1986) (see also Bernstein, 1974; Holland, 1978; McWilliams, 1985; Bane *et al.*, 1989; Meacham *et al.*, 1994, Danabasoglu *et al.*, 1994) oceanic perturbations are distinguished by their horizontal scale L relative to the Rossby deformation radius $L_R = \frac{\bar{N}H}{f}$ ($\bar{N}$ is the characteristic buoyancy frequency, H is the depth of the ocean, f is the Coriolis parameter). Namely, small-scale, mesoscale, synoptic scale, and global scale perturbations are characterized by $L \ll H$, $H < L < L_R$, $L \sim L_R$, and $L \gg L_R$, respectively. Note that the parameter L_R varies considerably in the ocean. For instance, it reaches 70–80 km in the tropic part of the Atlantic Ocean, and is much less in the arctic regions where $L_R \approx$ 5–10 km.

1. P. P. Shirshov Institute of Oceanology, Moscow, Russia.
2. Moscow Institute of Physics and Technology, Dolgoprudnyi, Moscow region, Russia.
3. V.I.Il'ichev Pacific Oceanological Institute, Vladivostok, Russia.
4. Far Eastern Federal University, Vladivostok, Russia.
5. Institute of Applied Mathematics, Vladivostok, Russia.
6. Corresponding author. ***email: kvkoshel@poi.dvo.ru***

Dynamics of synoptic and mesoscale vortices can be approximately described by one equation for the pressure P or for the stream function ψ, which are related by the linear relation $\psi = \frac{P}{\rho_0 f}$, where ρ_0 is characteristic density. The equation expresses conservation of the potential vorticity $q = \Delta\psi + \frac{\partial}{\partial z}\frac{f^2}{N^2}\frac{\partial \psi}{\partial z}$ and has the form (e.g. Monin *et al.*, 1977; Pedlosky, 1987)

$$\frac{\partial}{\partial t}q + J(\psi, q) = 0 \text{ or } \frac{d_h}{dt}q = 0. \tag{1}$$

In (1) t is the time; z is the axis directed upward; x, y are the horizontal axes; N is the buoyancy frequency; $\Delta = \frac{\partial^2}{\partial x^2} + \frac{\partial^2}{\partial y^2}$ and $J(A, B) = \frac{\partial A}{\partial x}\frac{\partial B}{\partial y} - \frac{\partial A}{\partial y}\frac{\partial B}{\partial x}$ are the horizontal Laplace and Jacobi operators, respectively; $\frac{d_h}{dt} = \frac{\partial}{\partial t} + u\frac{\partial}{\partial x} + v\frac{\partial}{\partial y}$, where u, v are the horizontal velocity components. Eq. (1) is derived using the f-plane approximation ($f = f_0 = const$), and assuming the Rossby number to be small, $Ro = \frac{U}{f_0 \cdot L} \ll 1$. In what follows, for simplicity we assume the buoyancy frequency N to be constant and neglect the influence of the β-effect (McWilliams, 1976; Fedorov and Ginzburg, 1986; Ivanov *et al.*, 1986; Reznik, 1992) on the vortex core deformation and effects related to the deformation.

With a knowledge of the stream function $\psi(x, y, z, t)$, one can calculate the horizontal velocity components (u, v),

$$u = -\frac{\partial \psi}{\partial y}, v = \frac{\partial \psi}{\partial x}, \tag{2}$$

the vertical velocity, pressure and density fields (e.g. Pedlosky, 1987).

According to observation synoptic/mesoscale eddy consists of a rotating vortex core and exterior fluid, involved in a rotational motion (Meacham *et al.*, 1994; Zhmur, 1988a, b; Dahleh, 1992; Kawakami and Funakoshi, 1999; Rom-Kedar *et al.*, 1990; Budyansky *et al.*, 2004; see also review by Koshel and Prants, 2006). The fluid inside the vortex core is slightly mixed with the exterior fluid and is transported along with the core. Following Thomson (1867), the volume of the trapped fluid is referred to as "vortex atmosphere." Usually the vorticity inside the core differs greatly from the vorticity of background exterior fluid.

Here we are interested in ellipsoidal vortices considered in a number of works (Zhmur, 1989; Zhmur and Pankratov, 1989, 1990a; Zhmur and Shchepetkin, 1991; Pankratov and Zhmur, 1991; Meacham, 1992, Meacham *et al.*, 1994; Muyazaki *et al.*, 1999, 2001; Dritschel *et al.*, 2004; Dritschel, 2010). These papers focus on the dynamics of mesoscale vortices: their rotation, deformation, interaction, and evolution in exterior flows of different kinds. The amount of the fluid carried out by the vortices is poorly known despite the apparent simplicity of the problem. If the induced velocity field is nonstationary, then the Lagrangian trajectories of fluid particles can be chaotic (Aref, 1990, 2002; Meleshko and Aref, 1996; Zaslavsky, 2007; Kozlov and Koshel, 1999, 2000; Koshel and Prants, 2006; Kozlov *et al.*, 2005; Prants *et al.*, 2006). In this case, the vortex atmosphere can entrain or detrain water mass.

The focus of this paper is the fluid advection (including chaotic advection) in velocity field induced by an ellipsoidal vortex. We pay special attention to localized regimes of the core motion, so we examine in sufficient detail the classification of these regimes obtained by Zhmur and Pankratov, (1990a,b), Zhmur and Shchepetkin (1991, 1992) and Meacham *et al*. (1989).

Chaotic behavior of the Lagrangian trajectories of the fluid particles has been demonstrated by Polvani and Wisdom (1990); Dahleh (1992); Kawakami and Funakoshi (1999); Shariff *et al.*(2006) and Chaplygin (2007) and Kida (1981) for a barotropic elliptic vortex. These works mainly study particular cases of a strong strain component. Again, the chaotization mechanism has not been clarified, with the exception of estimating the Melnikov integral, which relates only to the separatrix chaotic layer. In this paper we examine all characteristic types of the localized motion of an ellipsoidal vortex and study the formation mechanisms of both a separatrix chaotic layer and a strong chaos case (Koshel, *et al*., 2008; Izrailsky, 2006, 2008).

2. Model of ellipsoidal vortex

So, we consider the vortex with piece-wise constant potential vorticity (PV) q equal $2\alpha/2\beta$ inside/outside the vortex core ($\alpha \neq \beta$). The fluid is assumed to be infinite in all directions, i.e. the influence of the oceanic boundaries (both vertical and horizontal) is neglected (Zhmur, 1989). In this model the vortex dynamics is fully determined by evolution of the boundary of the vortex core which is conveniently represented by the equation

$$F(x, y, z, t) = 0.$$

Let the initial core be an ellipsoid and one of the ellipsoid axes is parallel to the z-axis. The background flow is assumed to be purely horizontal and linearly dependent on coordinates:

$$u_b = ex - \gamma y,\ v_b = \gamma x - ey; \tag{3}$$

the parameters e, γ are constant. Thus, we model the behavior of a mesoscale vortex embedded in a large-scale background flow. This problem was considered in a number of papers (Zhmur, 1989; Zhmur and Pankratov, 1989, 1990a; Zhmur and Shchepetkin, 1991; Pankratov and Zhmur 1991; Meacham *et al.*, 1994). The stream function corresponding (3) has the form $\psi_b = (x^2 + y^2)\gamma/2 - exy$, i.e. the background flow is a superposition of the rotation component $\gamma(x^2 + y^2)/2$ accelerating or decelerating rotation of the vortex, and the straining component $-exy$ forcing the vortex to elongate. Relative strength of these components is determined by the ratio e/γ, in the case $|e/\gamma| = 1$ the velocity field (3) being a rectilinear shear flow directed at an angle 45° to the x-axis.

Intrinsic dynamics of the vortex and interaction with this exterior flow results in that the vortex core is deformed in the horizontal plane and simultaneously rotates about the vertical axis (for more details see Meacham *et al.*, 1994). The boundary of the ellipsoidal

core remains ellipsoid; the vertical axis of the ellipsoid being constant and the horizontal axes changing in time. The equation which determines the boundary evolution can be written in the form:

$$F(x, y, z, t) = \frac{\tilde{x}^2}{a^2(t)} + \frac{\tilde{y}^2}{b^2(t)} + \frac{\tilde{z}^2}{c^2} - 1 = 0, \tag{4}$$

where the coordinates $(\tilde{x}, \tilde{y})$ are related to the coordinates (x, y) by equations

$$\begin{aligned} \tilde{x} &= (x - x_0)\cos\theta(t) + (y - y_0)\sin\theta(t), \\ \tilde{y} &= -(x - x_0)\sin\theta(t) + (y - y_0)\cos\theta(t). \end{aligned} \tag{5}$$

Here the fixed point x_0, y_0 corresponds to the vortex center, a and b are the principal horizontal semi-axes of the ellipsoid (by definition, a is the major semi-axis), c is the principal vertical semi-axis, θ is the angle between a and the x-axis. Dynamics of the core is described by the equations (see Zhmur and Pankratov, 1989):

$$\begin{aligned} &\dot{a} = ae\cos 2\theta, \quad \dot{b} = -be\cos 2\theta, \\ &\dot{\theta} = \Omega + \gamma - \frac{a^2 + b^2}{a^2 - b^2} e \sin 2\theta, \end{aligned} \tag{6}$$

where Ω is the natural rotation of the core in the absence of background flow,

$$\Omega = gab\tilde{c} \int_0^\infty \frac{\mu d\mu}{(a^2 + \mu)(b^2 + \mu)\sqrt{\Delta(\mu)}} = gK \int_0^\infty \frac{\mu' d\mu'}{[(\mu'^2 + \xi\mu' + 1)^3 (K^2 + \mu')]^{1/2}}, \tag{7}$$

and $\Delta(\mu) = (a^2+\mu)(b^2+\mu)(\tilde{c}^2+\mu), \xi = \frac{a}{b}+\frac{b}{a} = \varepsilon+\frac{1}{\varepsilon}, \tilde{c} = \frac{N}{f}c, K = \frac{\tilde{c}}{\sqrt{ab}}, 2g = 2(\alpha-\gamma)$. The parameter ξ describes the horizontal elongation of the core, K characterizes the vertical flatness of the core, and $\varepsilon = a/b$ is the horizontal aspect ratio of the ellipsoid.

We also need to calculate the stream function. It is convenient to write the stream function as a sum $\psi = \psi_b + \psi_V$, where ψ_V is the perturbation due to the vortex. These components satisfy the equations

$$\Delta\psi_b = 2\gamma, \Delta\psi_V = \begin{cases} 0, & \mathbf{r} \notin V, \\ 2g, & \mathbf{r} \in V. \end{cases}$$

For the vortex part we have (see Zhmur and Pankratov, 1989; Meacham *et al.*, 1994)

$$\psi_V(\tilde{x}, \tilde{y}, \eta) = -\frac{1}{2} gab\tilde{c} \int_{\lambda(\tilde{x},\tilde{y},\eta)}^\infty \left(1 - \frac{\tilde{x}^2}{a^2 + \mu} - \frac{\tilde{y}^2}{b^2 + \mu} - \frac{\eta^2}{\tilde{c}^2 + \mu}\right) \frac{d\mu}{\sqrt{\Delta(\mu)}}. \tag{8}$$

For the fluid particles located inside the core, the parameter λ in (8) should be taken as zero. For the exterior fluid particles, including the boundary, $\lambda(\tilde{x}, \tilde{y}, \eta) \geq 0$ is the positive root of the equation

$$\frac{\tilde{x}^2}{a^2+\lambda} + \frac{\tilde{y}^2}{b^2+\lambda} + \frac{\eta^2}{\tilde{c}^2+\lambda} = 1. \tag{9}$$

Horizontal velocity components $(\tilde{u}, \tilde{v})$ in the rotating coordinates $(\tilde{x}, \tilde{y})$ have the form

$$\tilde{u} = -\frac{\partial}{\partial \tilde{y}}\psi_V = -gab\tilde{c}\int_{\lambda}^{\infty} \frac{d\mu}{(b^2+\mu)\sqrt{\Delta(\mu)}}\tilde{y}$$

$$\tilde{v} = \frac{\partial}{\partial \tilde{x}}\psi_V = gab\tilde{c}\int_{\lambda}^{\infty} \frac{d\mu}{(a^2+\mu)\sqrt{\Delta(\mu)}}\tilde{x}. \tag{10}$$

There are three dynamical regimes of the core behavior inside the flow in the horizontal plane: oscillation, rotation, and infinite elongation (Zhmur and Pankratov, 1989; Meacham *et al.*, 1994). When the oscillation or rotation regimes occur, the horizontal scales and the orientation of the core alter periodically. When infinite elongation occurs, one horizontal axis tends to infinity, while the other one tends to zero. Analogous regimes exist in the case of the barotropic elliptical vortex (Kida, 1981; Meacham *et al.*, 1989).

Below we use Eqs. (3)–(10) written in nondimensional form using the scales L, h, U, $\bar{N}$, the time scale $t^* = L/U$, and the stream function scale $\psi^* = UL$. Formally, the nondimensional equations coincide with the dimensional ones since we use the same notations for the dimensional and the nondimensional variables.

The equations governing the motion of fluid particle have the form

$$\frac{dx}{dt} = u = ex - \gamma y - \frac{\partial}{\partial y}\psi_v,$$

$$\frac{dy}{dt} = v = \gamma x - ey + \frac{\partial}{\partial x}\psi_v. \tag{11}$$

We introduce useful notations for elliptic integrals

$$\alpha_0 = abc\int_0^{\infty} \frac{1}{a^2+\mu}\frac{d\mu}{\sqrt{\tilde{\Delta}(\mu)}}, \quad \beta_0 = abc\int_0^{\infty} \frac{1}{b^2+\mu}\frac{d\mu}{\sqrt{\tilde{\Delta}(\mu)}}, \quad \chi_0 = abc\int_0^{\infty} \frac{d\mu}{\sqrt{\tilde{\Delta}(\mu)}}, \tag{12}$$

and expression for the frequency Ω obtained in Zhmur and Pankratov (1989):

$$\Omega = g\bar{\Omega} = -g\frac{\beta_0 b^2 - \alpha_0 a^2}{a^2 - b^2}. \tag{13}$$

The last terms in the right-hand side of Eq. (11) are calculated using (5), (10)

$$\frac{\partial}{\partial x}\psi_V = \cos\theta\frac{\partial}{\partial\tilde{x}}\psi_V - \sin\theta\frac{\partial}{\partial\tilde{y}}\psi_V,$$
$$-\frac{\partial}{\partial y}\psi_V = -\sin\theta\frac{\partial}{\partial\tilde{x}}\psi_V - \cos\theta\frac{\partial}{\partial\tilde{y}}\psi_V. \tag{14}$$

To calculate fluid particle trajectories one should solve the systems (6), (11) together with (4), (5), (9), (10), (13), (14). It readily follows from (6) that $a(t)b(t) = const$ (we recall that the vertical axis c is assumed to be constant). As a result, we have a dynamical system with two degrees of freedom for Lagrangian trajectories of fluid particles. It was proven that such a case of two degrees of freedom is nonintegrable, and the trajectories could manifest chaotic behavior (Amol'd, 1989; Wiggins, 1990).

3. Regimes of vortex's core motion

System (6) is conveniently reduced to two equations for ε, θ (Zhmur and Pankratov, 1989)

$$\dot{\varepsilon} = 2e\varepsilon\cos 2\theta, \quad \dot{\theta} = \Omega(\varepsilon) + \gamma - e\frac{\varepsilon^2+1}{\varepsilon^2-1}\sin 2\theta. \tag{15}$$

In its turn, it readily follows from (15) that

$$\frac{d\sin 2\theta}{d\varepsilon} = \frac{1}{\varepsilon}\left(\frac{\Omega(\varepsilon)+\gamma}{e} - \frac{\varepsilon^2+1}{\varepsilon^2-1}\sin 2\theta\right), \tag{16}$$

whence we have (Zhmur and Pankratov, 1989):

$$\sin 2\theta(\varepsilon) = \frac{\varepsilon}{\varepsilon^2-1}\left\{\frac{\varepsilon_0^2-1}{\varepsilon_0}\sin 2\theta_0 + \frac{1}{e}\int_{\varepsilon_0}^{\varepsilon}\frac{\tau^2-1}{\tau^2}\Omega(\tau)d\tau + \frac{\gamma}{e}\left(\varepsilon + \frac{1}{\varepsilon} - \varepsilon_0 - \frac{1}{\varepsilon_0}\right)\right\}, \tag{17}$$

where θ_0, ε_0 are some initial values. The integral in (17) may be expressed in a symmetric form of elliptic integral (Carlson and Gustafson, 1993; Dritschel *et al.*, 2004)

$$\sin 2\theta(\varepsilon) = \frac{\varepsilon}{\varepsilon^2-1}\left\{\frac{\varepsilon_0^2-1}{\varepsilon_0}\sin 2\theta_0 - \frac{g}{2eab}[\chi_0(a,b,c) - \chi_0(a_0,b_0,c_0)]\right.$$
$$\left. + \frac{\gamma}{e}\left(\varepsilon + \frac{1}{\varepsilon} - \varepsilon_0 - \frac{1}{\varepsilon_0}\right)\right\}. \tag{18}$$

We now consider phase portraits on the phase plane $(\varepsilon, \sin 2\theta)$ of the system in detail. Phase trajectories satisfy Eq. (17), but it is more convenient to use (15) for the analysis of stagnation points. The initial position (0,1) gives a hyperbolic point. The axis $\varepsilon = 1$ is the

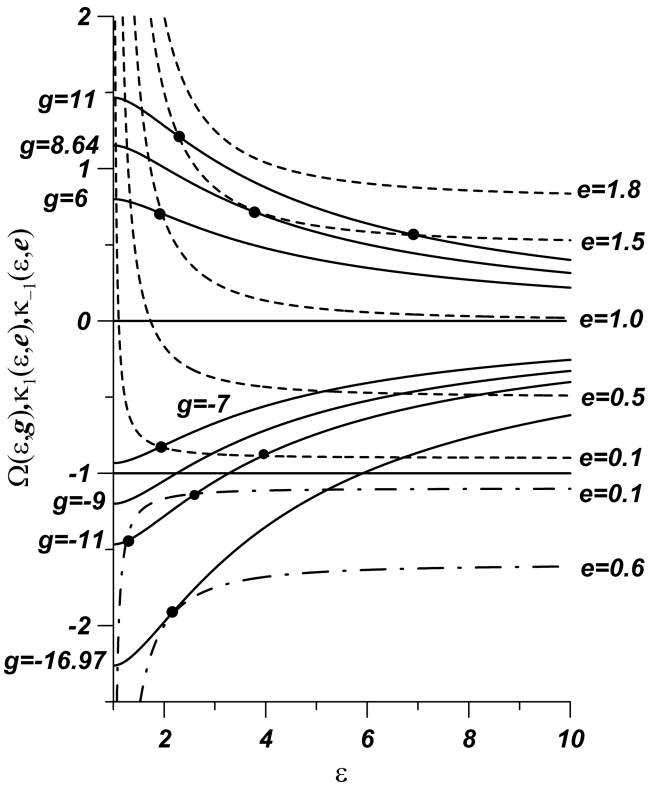

Figure 1. $\Omega(\varepsilon)$ (solid lines), $\kappa_1(\varepsilon)$ (dashed lines), and $\kappa_{-1}(\varepsilon)$ (dot-dashed lines) as functions of ε at specified values of e and g for $K = 1$. The black circles show graphical solutions of equations (20).

first branch of the separatrix for this point. The second branch can be described by equation (18) for $\theta_0 = 0$, $\varepsilon_0 = 1$ (Zhmur and Pankratov, 1989):

$$\sin 2\theta(\varepsilon) = -\frac{g}{eab}\frac{\varepsilon}{\varepsilon^2-1}[\chi_0(a,b,c) - \chi_0(a_0, b_0 = a_0, c)] + \frac{\gamma}{e}\frac{\varepsilon-1}{\varepsilon+1}. \qquad (19)$$

It is obvious that $\dot{\varepsilon} = 0$ when $\sin 2\theta = \pm 1$; also, when g is negative, $\dot{\theta}$ may be zero in one or two points when $\sin 2\theta = -1$, and only in one point when $\sin 2\theta = 1$. When g is positive and $\sin 2\theta = 1$, there are one or two stationary points, and when $\sin 2\theta = -1$, the stationary points are absent. Coordinates of the stationary points satisfy the equations

$$e\frac{\varepsilon^2+1}{\varepsilon^2-1} = \Omega(\varepsilon) + \gamma, \quad \sin 2\theta = 1; \quad -e\frac{\varepsilon^2+1}{\varepsilon^2-1} = \Omega(\varepsilon) + \gamma, \quad \sin 2\theta = -1. \qquad (20)$$

Below we normalize g, e by γ, i.e., by g and e, we mean g/γ and e/γ. Figure 1 represents the solutions of (20). It shows $\Omega(\varepsilon)$, $\kappa_1(\varepsilon) = e\frac{\varepsilon^2+1}{\varepsilon^2-1} - 1$, and $\kappa_{-1}(\varepsilon) = -e\frac{\varepsilon^2+1}{\varepsilon^2-1} - 1$ as

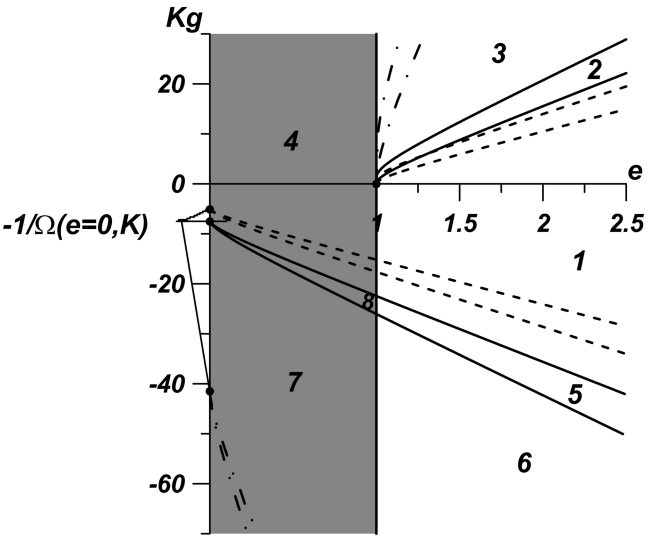

Figure 2. The regions for different regimes of vortex core motion on (gK, e)-plane. The solid lines correspond to $K = 1$. The dashed lines correspond to $K = 0.01$, and the dot-dashed lines, to $K = 10$. The white background corresponds to $e > 1$ with motion types of 1-3,5,6; the gray background corresponds to $e \leq 1$ with motion types of 4,7,8.

functions of ε. The intersection of the frequency line $\Omega(\varepsilon)$ with the line $\kappa_1(\varepsilon)$ gives the stationary points for $\sin 2\theta = 1$, and that with the line $\kappa_{-1}(\varepsilon)$ for $\sin 2\theta = -1$.

Let us analyze dependence of the number of stationary points on the parameters g, e. We start with the case $e > 1$, $g > 0$. When $g > 0$, the frequency lines begin with a finite value of $\Omega(1; K, g)$ and tend to zero when ε increases as $|\Omega(\varepsilon)| \sim \ln \varepsilon / \varepsilon^{1/2}$ (Carlson and Gustafson, 1993). Thus, the frequency lines may intersect only the lines $\kappa_1(\varepsilon)$. It is seen from Figure 1 that given e, the frequency lines corresponding to too small g lay below the corresponding line $\kappa_1(\varepsilon)$; i.e., there are no stationary points in this case. With increasing g the frequency line becomes tangent to the curve $\kappa_1(\varepsilon)$, and then, with further increase of g, either one (as, for example, for $g = 6$, $e = 1$) or two (as, for example, for $g = 8.64$, $e = 1.5$) stationary points appear, for all these points $\sin 2\theta = 1$.

Figure 2 shows the curve $g(e)$, corresponding to the case of tangency; the line separates regimes 1 (no stationary points) and 2 (two stationary points). As the frequency line decreases slower than the dashed line, we have only one intersection when $e = 1$; i.e., the line separating regimes 1 and 2 starts from the initial position $g = 0$, $e = 1$.

In the case $e > 1$, $g < 0$ the frequency lines are negative and cannot intersect the positive dashed lines $\kappa_1(\varepsilon)$, i.e. there are no stationary points when $\sin 2\theta = 1$. The case of lines $\kappa_{-1}(\varepsilon)$ and negative g is analogous to the case of lines $\kappa_1(\varepsilon)$ and positive g. When the absolute value of g is small, the frequency line lays above the dot-dashed line (for example, $g = -15$, $e = 0.6$); i.e., there are no stationary points for $\sin 2\theta = -1$. With increasing

absolute value of g given e, at first, a tangency point (for example, for $g = -16.97, e = 0.6$), and then two intersection points, appear. The line, corresponding to the tangency, is shown in Figure 2, where it separates regimes 1 (above), and 5 (below).

Figure 3a illustrates the phase portrait on the plane (ε, $\sin 2\theta$) for the vortex core motion in regime 1 (no stationary points). The separatrix, which starts at (0,1), asymptotically tends to the limit $1/e$ with increasing ε, and it may have a maximum (minimum) when g is positive (negative). The phase trajectories are confined to the strip $\sin 2\theta = \pm 1$ and begin either at the boundary $\sin 2\theta = 1$ or at the boundary $\sin 2\theta = -1$.

There is no stationary points on the boundaries $\sin 2\theta = \pm 1$ in the regime 1, therefore all trajectories run to infinity when ε increases. Thus, in this case, we have an infinitely elongating vortex core, and there are no localized motions. Figure 3a shows the separatrices for zero and negative g, which demonstrate that the phase trajectories may be slightly deformed, but there are still no localized motions.

The stationary points on the upper or lower boundaries of the physical space exist in the regimes 2 and 5. These points correspond to two intersections of the frequency lines with the dashed and dot-dashed lines as shown in Figure 1. Figure 3b demonstrates a phase portrait when g is positive (regime 2). The second stationary point (marked by cross) corresponds to a maximum of phase line lying above the separatrix. It is not a hyperbolic point, so it corresponds to tangency of phase line and boundary of physical region, but not an intersection of two phase trajectories. We call this phase line pseudoseparatrix because it separates phase trajectories corresponding to different regimes of the core motion (oscillation, elongation, and, for some special cases, rotation). The pseudoseparatrix is tangent to the upper boundary of the physical region; the phase trajectories which begin on the left to the tangency point intersect the upper boundary twice, and there is an elliptic stationary point in any case. This point corresponds to zero angular velocity of the vortex core, the angle θ being given by the equation $\sin 2\theta = 1$. The vortex motion along the phase trajectories that intersect the boundary $\sin 2\theta = 1$ twice occurs with rebounding; i.e., we have the oscillation regime in the region left to the pseudoseparatrix tangency point. So, in this case we have oscillation regimes above and left of the pseudoseparatrix, and elongation regimes above and right of it. Between the separatrix and the pseudoseparatrix, the elongation starts from the upper boundary, the pattern of the elongation coinciding with the pseudoseparatrix. Below the separatrix, the elongation starts from the bottom boundary $\sin 2\theta = -1$ but does not approach the upper boundary, the limiting angle of rotation θ_0 is given by the equation $\sin \theta_0 = 1/e$.

Figure 3c represents a phase portrait of the regime 5 ($g < 0$). This regime is analogous to the regime 2 with the difference that the separatrix has a minimum (not maximum), and therefore the pseudoseparatrix is tangent to the bottom boundary, which results in that the localized motions (oscillations) take place in the vicinity of the angle θ satisfying $\sin 2\theta = -1$.

In the above regimes 1, 2, 5 the separatrix does not approach the boundaries $\sin 2\theta = \pm 1$. When the absolute value of g increases given $e > 1$, the separatrix at first becomes tangent

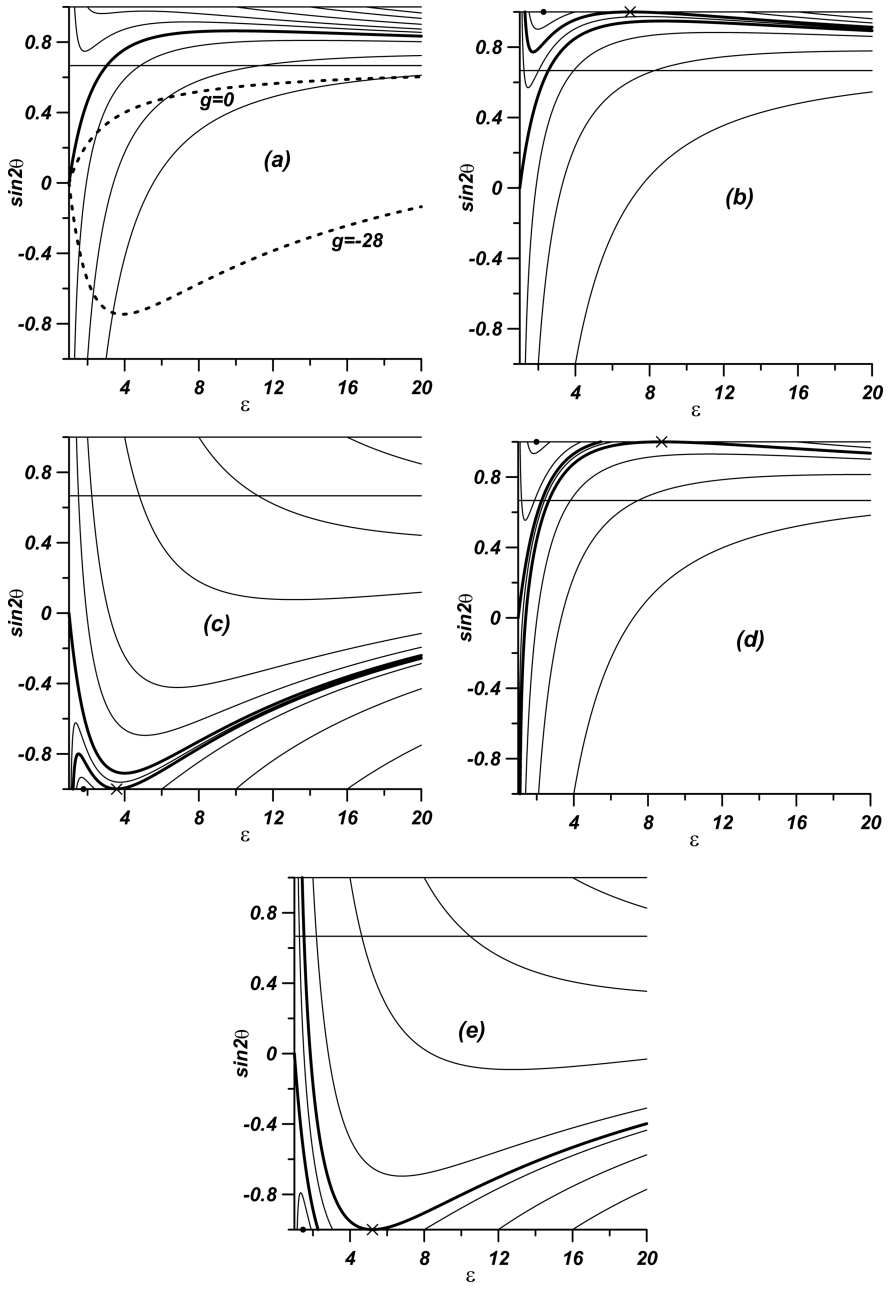

Figure 3. Phase trajectories on the plane $(\varepsilon, \sin 2\theta)$ for $K = 1$, $e = 1.5 > 1$. (a) $g = 8.75$, regime 1; (b) $g = 11$, regime 2; (c) $g = -32$, regime 5; (d) $g = 13$, regime 3; (e) $g = -40$, regime 6. The bold lines are separatrices. The horizontal line marks the level of $1/e$. All trajectories that do not intersect the line $\sin 2\theta = \pm 1$ tend to the level $1/e$.

to the upper or lower boundary and intersects the boundary with further increasing g. When the separatrix intersects the boundary, the pseudoseparatrix is tangential to the boundary on the right of the separatrix. Figure 2 shows two lines of $g(e)$, which correspond to the tangency of the separatrix with the upper boundary (the line separating regimes 2 and 3) or the lower boundary (the line separating regimes 5 and 6).

Figure 3d represents a phase portrait of the regime 3. Like the regime 2, there are two stationary points on the upper boundary but in this case, separatrix intersects the boundary and the intersection point is located between these stationary points. Thus, the oscillation regime about the elliptic point takes place left and above the separatrix. The phase trajectories between the separatrix and the pseudoseparatrix start at the lower boundary and finish at the upper one. Finally, in the domain above the pseudoseparatrix and on the right of the second stationary point (cross), and in the domain below of the pseudoseparatrix, the phase trajectories go to infinity. The phase portrait of the regime 6 ($g < 0$) shown in Figure 3e is analogous to the regime 3 if one exchanges the upper and the lower boundaries.

We now consider the case $e < 1$. In this case the asymptotic limit of all trajectories $1/e$ lies outside the physical region; i.e., all phase trajectories intersect either the upper or the lower boundary $\sin 2\theta = \pm 1$ and no trajectories go to infinity. For positive g only one stationary point on the upper boundary exists because the dashed lines in Figure 1 asymptotically tend to the negative limit $e - 1$. If g is negative and small enough in absolute value, then the negative frequency lines in Figure 1 lie above the dot-dashed lines and intersect the dashed lines (as for example, for $g = -7$, $e = 0.1$); i.e., there is only one stationary point on the upper boundary in this case. We will refer to this regime as the regime 4 (see Fig. 2).

An example of the phase portrait for the regime 4 is shown in Figure 4a. The separatrix intersects the upper boundary and the phase trajectories in the domain above and on the left of the separatrix corresponds to the oscillation regime. On the right of the separatrix all phase trajectories start at the lower boundary and finish at the upper one, so we have only rotation regime here.

For comparison, we show the separatrix with negative $g = -10$, which has a minimum at negative $\sin\theta$. With increasing absolute value of g this minimum shifts to the lower boundary which finally results in an arising pseudoseparatrix tangent to this boundary as shown in Figure 4b. This figure represents the regime 8 which is separated from the regime 4 by continuation to the domain $e < 1$ of the line separating the regimes 1 and 5 in Figure 2. Like the regime 4, the motion can be only localized in the regime 8 since all phase trajectories start and finish at the boundaries. This regime is characterized by rather large negative g and $e < 1$. The corresponding negative frequency line in Figure 1 intersects the dot-dashed line in two points and the dashed line in one point. Thus there are two stationary points on the lower boundary and one stationary point on the upper one. As a result the regime 8 is characterized by the oscillation regime above the separatrix, the rotation regime between the separatrix and the pseudoseparatrix, another oscillation regime on the left of and below the pseudoseparatrix, and another rotation regime on the right of the pseudoseparatrix. Amplitude of the oscillations of the vortex near the direction $\sin 2\theta = 1$

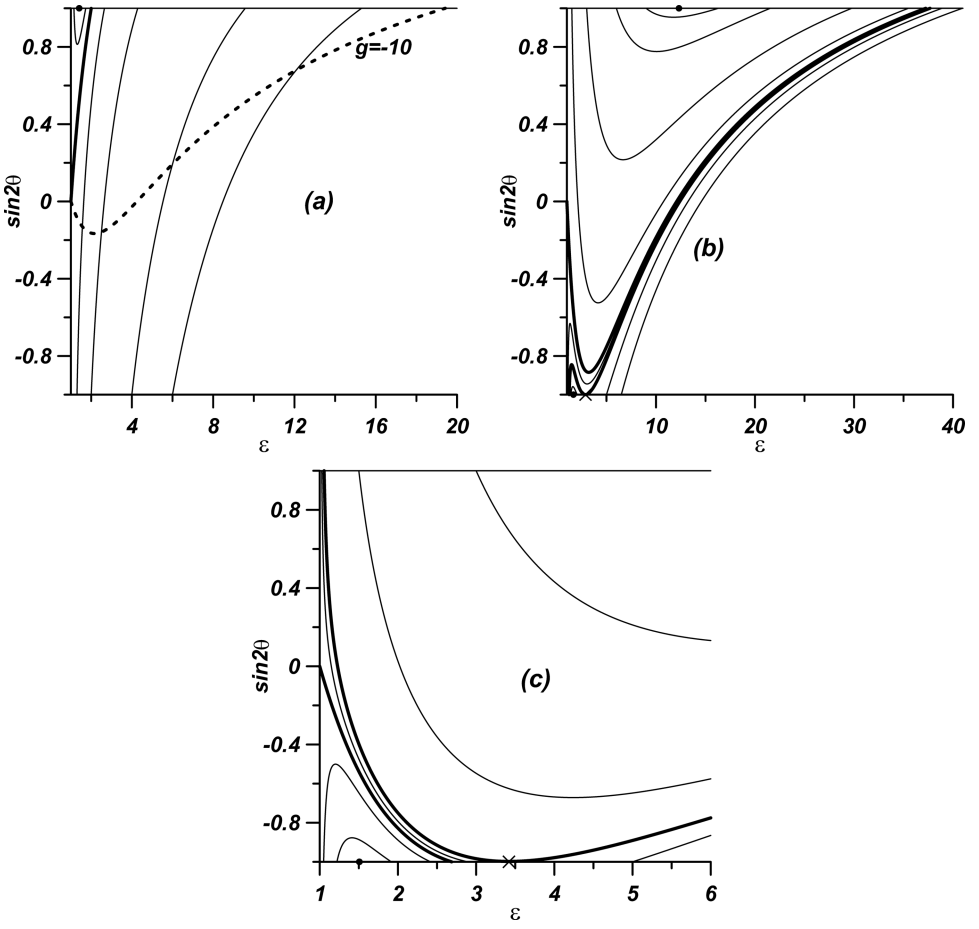

Figure 4. Phase trajectories on the plane (ε, sin 2θ), when $K = 1$, $e = 0.5 < 1$. (a) $g = 4$, regime 4; (b) $g = -16.7$, regime 8; (c) $g = -18$, regime 7. The bold lines are the separatrices.

(upper boundary) can greatly exceed the corresponding amplitude of the oscillations near the direction $\sin 2\theta = -1$ (lower boundary). The phase trajectories between the separatrix and the pseudoseparatrix describe an interesting regime of motion when the system passes through half of an oscillation period, then a revolution occurs, after which another half of the oscillation period takes place.

As in the case $e > 1$, further increasing absolute value of the negative g given $e < 1$ results in that the separatrix, at first, becomes tangent to the lower boundary and then intersects the boundary which characterized the regime 7 shown in Figure 4c. In Figure 2 the line separating the regimes 5 and 6 prolongs to the region of $e < 1$, where it separates the regimes 7 and 8. The regime 7 differs from the regime 6 in that all the trajectories above the pseudoseparatrix start and finish at the upper boundary (not shown in Fig. 4c).

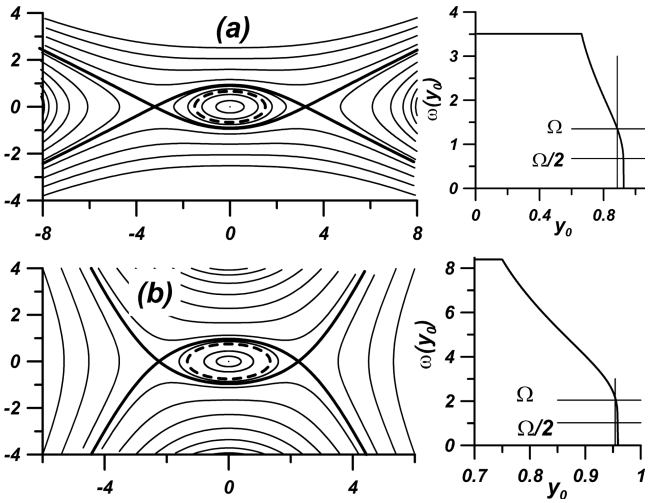

Figure 5. Fluid particle trajectories in the velocity field induced by a vortex core ($K = 1, e = 1.5$) located in the elliptic point shown in (a) Figure 3b, $g = 4$, $\varepsilon_0 = 2.28$ and (b) Figure 3c, $g = -32$, $\varepsilon_0 = 1.78$. The bold lines correspond to the separatrices, and the bold dashed lines correspond to the vortex core boundary. The mean rotation frequencies of fluid particles are given on the right.

We now consider the case $e = 1$ which corresponds to a purely shear flow directed along the line $y = x$. It is seen from Figure 1 that for positive g, only a stationary point exists on the upper boundary so this is the fourth regime. The separatrix intersects the upper boundary at some finite ε and the intersection point goes to infinity as $g \to 0$. When g is negative $\kappa_1(\varepsilon) > 0$ and we have the first, fifth, and sixth regimes for $e = 1$.

Let us briefly discuss the influence of parameter K on the motion regimes. Absolute value of the frequency decreases with the decreasing of K; hence, the maximal value of the lines separating the fourth, eighth, and seventh regimes also diminishes with decreasing K. Therefore, the lines separating the first, second, and third regimes shift upward, and consequently the slope of these lines increases. In general, changes in the motion regimes will occur at greater absolute values of g. Figure 2 demonstrates plots of $Kg(e)$ for $K = 0.01$ (the dashed lines) and $K = 10$ (the dot-dashed lines).

4. Velocity field induced by the ellipsoidal vortex

We now analyze the velocity field induced by an ellipsoidal vortex embedded in a nonuniform flow and Lagrangian trajectories inside the field. The analysis is confined to the cases of localized motion of the vortex (i.e., oscillations and rotations), and the regimes of chaotization of the Lagrangian trajectories are of special interest. Below we show that the rotation regimes induce velocity fields analogous to those induced by the oscillation regimes.

We start with a steady-state case which corresponds to the elliptic stationary point in the phase portrait (e.g. Fig. 3b). Figure 5 displaces the streamlines in this case for $e > 1$ when

the background strain dominates over the background rotation. The streamline field consists of the central vortex part with closed streamlines surrounded by four domains where the motion is not localized and the streamlines start and finish at infinity. In Figure 5b the vortex amplitude is larger than in Figure 5a; therefore, the streamline pattern in Figure 5a is more elongated along the x-axis.

If $e < 1$ (background rotation dominates over background strain) the streamline pattern is very different from the above one, as shown in Figure 6. In this case the streamlines are always closed, and their shape depends on the sign of g determining the relative strength of the vortex and the external rotation. In the case $g > 0$ all trajectories are limited and surround the vortex core as shown in Figure 6a. When g is negative the dynamics change (Figs. 6b and 6c). Near the vortex core the motion is determined by the core rotation; however, far away from the core the fluid particle dynamics is dominated by the external flow and the particle trajectories tend to ellipses determined by the external flow. When the effects of the core and of the external flow are in balance, stationary points and, therefore, a separatrix emerges.

Frequency of rotation of a fluid particle around the vortex core is of use for the analysis of trajectory behavior within the external nonstationary flow. Motion of the particle is, generally, nonuniform and therefore we determined this frequency as averaged angular velocity $\omega(y_0) = 2\pi/T$, where T is the period for the fluid particle trajectory in the coordinates x, y, and y_0 is an initial position of the particle. Figures 5 and 6 show the rotation frequencies as functions of the initial positions.

The frequencies are constant inside the core; here the solid-state rotation with double rotating frequency of the vortex core shape takes place (Zhmur and Pankratov, 1989). When $e > 1$, the frequencies rapidly decrease from the core boundary to the separatrix. When $e < 1$, the rotation frequencies tend to the frequency determined by the external flow $\omega_\infty = \sqrt{\gamma^2 - e^2}$ with increasing $|y_0|$. For positive g the frequencies decrease monotonically from the core boundary to the level ω_∞. For negative g the situation is more complicated. As mentioned above, the frequencies are positive and are determined by the external flow at large distances from the core, while they are negative and are determined by the core motion in the vicinity of it; furthermore, the frequencies are zero at the separatrices. Such distribution of the frequencies results in that there are a few trajectories that have the same frequencies, the fact that is crucial for chaotic dynamics formation (Koshel *et al.*, 2008).

5. Nonstationary regimes of vortex motion and chaotic advection

If the motion is nonstationary, for example, the vortex oscillates in the vicinity of elliptical point, solutions of (15) depend on time and the particle trajectories are described by nonautonomous dynamic system (11). Such systems are known as systems with one and a half degrees of freedom, and they admit arising dynamical chaos (Zaslavsky, 2007). If amplitude of the oscillations is small and there is a separatrix in the stationary velocity field, then a stochastic layer arises near the separatrix in the corresponding nonstationary velocity

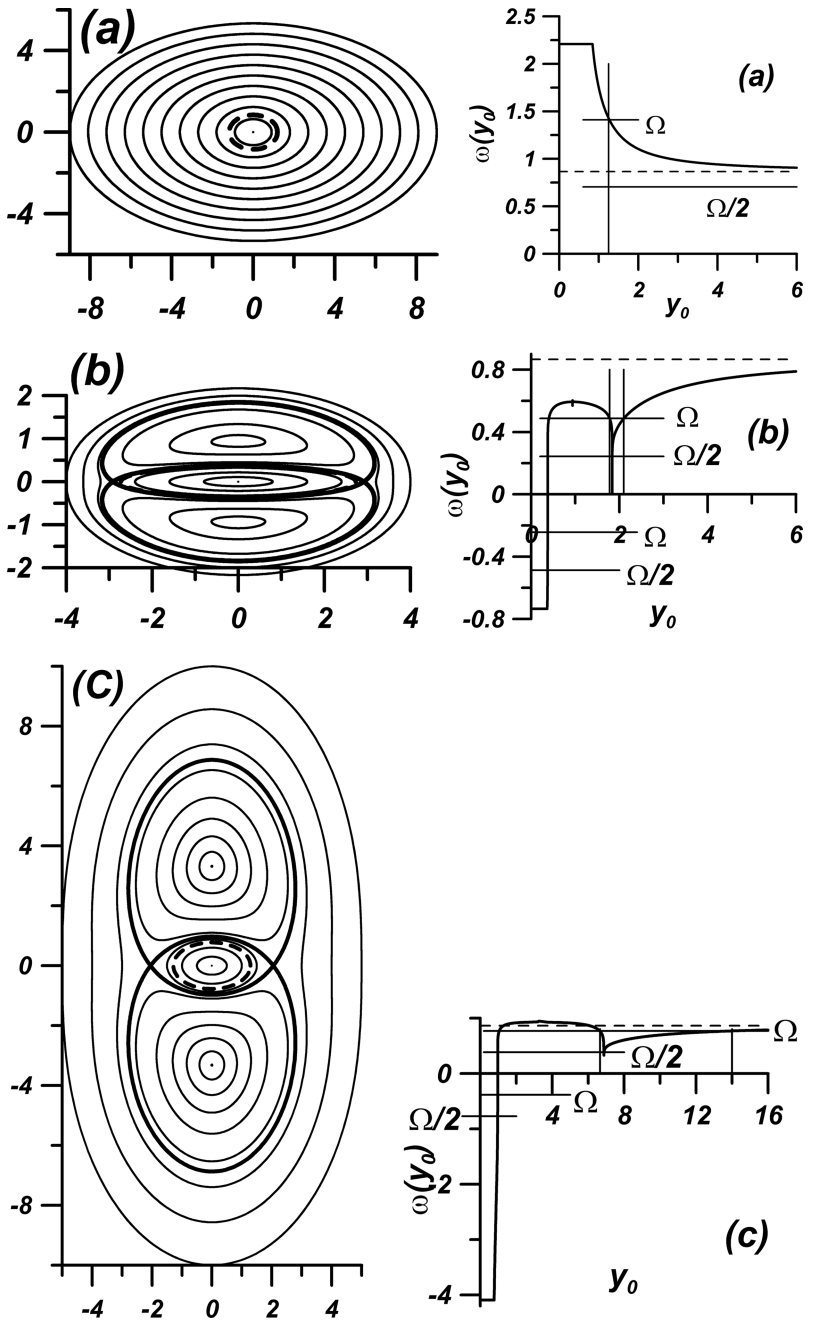

Figure 6. Fluid particle trajectories in a velocity field induced by a vortex core ($K = 1, e = 0.5$) located in the elliptic point shown in (a) Figure 4a ($g = 4, \varepsilon_0 = 1.41$); (b) 4a ($g = -10, \varepsilon_0 = 7.46, \sin 2\theta_0 = 1$), (c) 4b ($g = -16.7, \varepsilon_0 = 1.66, \sin 2\theta_0 = -1$).

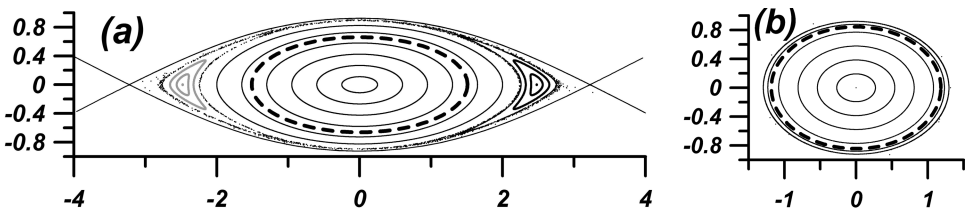

Figure 7. Poincare sections for parameters same as in Figures. 3b and 5a ($K = 1$, $g = 11$, $e = 1.5$), and the initial values of ε_0 : (a) $\varepsilon_0 = 2.241$; (b) $\varepsilon_0 = 1.4$

field. Also nonlinear resonances may appear in such a nonstationary field and separatrices of the nonlinear resonances may generate chaotic behavior. With increasing the oscillation amplitude the nonlinear resonances start to overlap, resulting in appreciable chaotization in the area of overlapping. Analysis of nonlinear resonances in geophysical flows is discussed in a number of papers (see for example, del-Castillo-Negrete and Morrison, 1993; Gudimenko, 2007; Izrailsky *et al.*, 2006, 2008; Koshel *et al.*, 2008; Ryzhov and Koshel, 2010; Ryzhov *et al.*, 2010).

To estimate the size of the area in which the nonlinear resonances arise, we show in Figures 5 and 6 the frequency Ω of oscillations of the core when it slightly deviates from the elliptic point. The level $\omega = \Omega$ intersect frequency line $\omega(y_0)$ at the point y_0 corresponding to a resonance trajectory with the winding number of 1:1. The levels of half-frequency $\omega = \Omega/2$ are also shown. Intersection of these levels with the frequency lines corresponds to the resonance trajectories with the winding number of 1:2.

We now consider the appearance of nonlinear resonances when the core slightly deviates from the elliptic point. We start with the case shown in Figure 5a. Here the resonance trajectories are located near the separatrix therefore the chaotization is rather weak but the mechanism of arising chaos is seen clearly. Figure 7 demonstrates Poincare sections which show the positions of a trajectory once per period of the vortex core oscillation. According to Figure 5a, one can see the appearance of a pair of resonances 1:1 near the separatrix. To show that these are exactly the resonances 1:1, we use different gray scales to mark two fluid particles that start from different stability islands. One can see that the marker from one stability island cannot be caught by another one. Since the resonances are located near the separatrix they are partially destroyed, and the fluid outside the stability islands flows out to the exterior flow domain because of chaotic advection. An interesting feature of Poincare sections in Figure 7a is a narrow stochastic layer between the resonances and core vicinity.

With increasing amplitude of the core oscillations the nonlinear resonances more and more lap over the separatrix stochastic layer and when the amplitude is nearly maximal, the resonances are completely destroyed. Additionally, owing to a decrease in the rotation frequency, the resonances or the area of their destruction move toward the separatrix layer. The maximal chaotization (with regular area near core boundary $\sim$0.1 width) is reached when the amplitude of the oscillation is almost maximal. In the regime 3 of the vortex

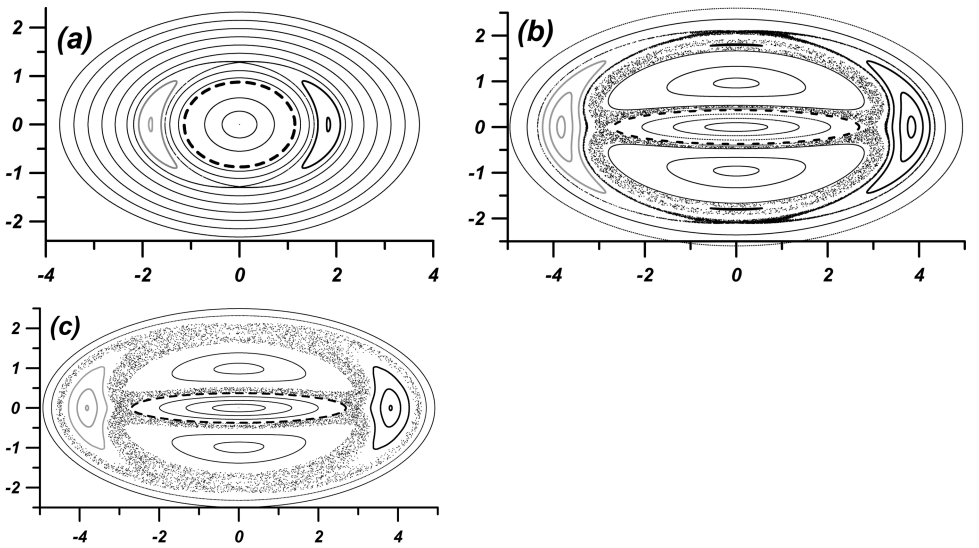

Figure 8. Poincare sections for parameters same as in Figures 6a, b ($K = 1, e = 0.5$), and initial values of ε_0 : (a) $\varepsilon_0 = 1.31$, $g = 4$; (b) $\varepsilon_0 = 7.25$; $g = -10$ (c) $\varepsilon_0 = 7.0$, $g = -10$.

motion we see analogous dynamics. As seen from Figure 5b, in this case the resonances are closer to the separatrix than in the preceding case and, therefore, the regular zone in the vicinity of the core is larger when the maximal chaotization occurs (see Fig. 7b).

Much more diverse effects of the chaotic advection arise in the case of $e < 1$. For positive g the rotation frequency decreases slowly with increasing distance from the core. Therefore the nonlinear resonances are separated by sufficiently large distances and the resonance widths decrease (Koshel *et al.*, 2008), so there is only a pair of 1:1 resonances and a narrow separatrix layer (see Fig. 8a). When g is negative, the recirculation zones arise and the frequency lines become more complicated (see Figs. 6b,c); the frequency of the vortex oscillation (rotation) is less than the maximal frequency of a fluid particle since the vortex is slowed down by the external flow.

One can see from Figure 6 that four pairs of 1:1 resonances can be expected: one between the core boundary and the separatrix, two inside the recirculation zones (one pair per zone); and one in the flow exterior outside the separatrix. Figure 8 represents an example of the motion regime 4 for negative g. We see all resonance pairs corresponding to the frequency line, except for the pair which is nearest to the core boundary. This pair is completely destroyed even in the presence of such a weak perturbation. On the whole, since the resonances are quite close to the separatrix, all of them are partially destroyed which results in the appearance of a large chaotic zone with strong mixing. Due to closeness of the separatrix to the core boundary and the existing nonlinear resonances in this narrow domain, the boundary of the chaotic zone is located near the core boundary. Maximal chaotization

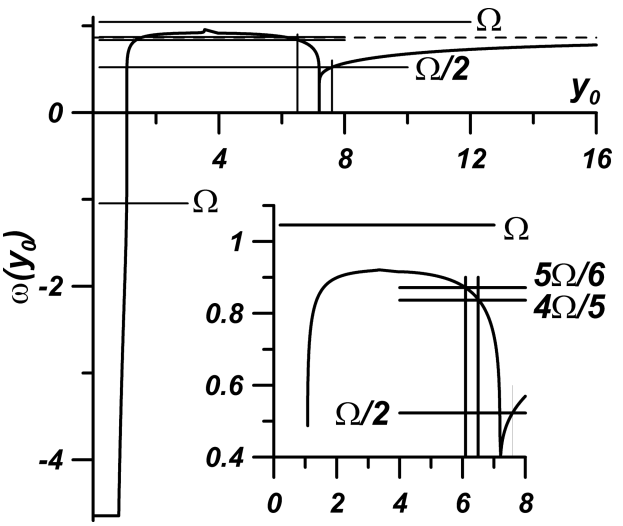

Figure 9. The frequencies of fluid particle rotation as functions of the initial position of the particle on the semimajor axis. Ω is the mean oscillation frequency of the core. The dashed line marks the rotating frequency of a fluid particle in the absence of the core $\sqrt{\gamma^2 - e^2}$. The parameters correspond to Figure 4c.

takes place when the perturbation amplitude is almost maximal; in this case, the widths of resonances increase but they come closer to the separatrix because of a decrease in the oscillation frequency with increasing amplitude. Minimal width of the regular region is ∼0.014. Figure 8c shows the dynamics of the regime 8, which is analogous to that of the regime 4 for negative g. Velocity field induced in the vicinity of the stationary point at $\sin 2\theta = -1$ for the regime 7 is analogous to that for the regime 8; therefore, we examine only the regime 7 that allows us to study both the oscillation and the rotation types of the vortex motion. An important point is that with increasing absolute value of g the frequency of the vortex core oscillation (rotation) also increases. Figure 9 shows the frequency curve for this case. For a large absolute value of g the maximal oscillation frequency exceeds the maximal frequency for recirculation zones and even the maximal rotation frequency determined by the external flow. Thus for small perturbations the widest resonances 1:1 can appear only in the domain between the core boundary and the separatrix. In the absence of the widest resonances one can see narrower resonances with fractional winding numbers (Koshel *et al.*, 2008).

An example for small perturbation amplitude in regime 7 is represented in Figure 10a. The domain of chaotization is bounded by four boundaries: one is in the vicinity of the core, another is in the external flow, and two are inside the recirculation zones. In all cases the location of the boundary is determined by the last undestroyed resonance. In the external flow these are the resonances 1:2 (one of them is marked by a blue marker, and another by a dark blue marker), which are located quite close to the separatrix (see Fig. 9). In

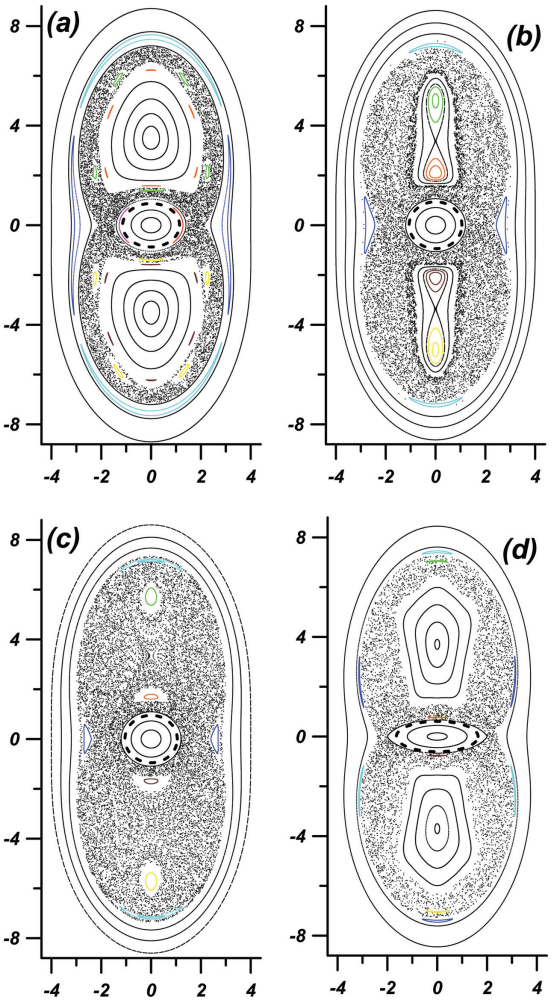

Figure 10. Poincare sections with parameters corresponding to Figure 4c ($K = 1, g = -18, e = 0.5, \sin 2\theta_0 = -1$) for different amplitudes of vortex oscillations, ε_0: (a) $\varepsilon_0 = 1.307$, (b) $\varepsilon_0 = 1.27$, (c), $\varepsilon_0 = 1.1$ (d) $\varepsilon_0 = 2.7$ (rotation). The vortex core is at rest when, $\varepsilon_0 = 1.507$.

the core vicinity these are very narrow (Ryzhov and Koshel, 2010; Ryzhov *et al.*, 2010) resonances 1:1 (red and magenta). In the recirculation zones all resonances are destroyed except for the resonances 5:6 (orange in one zone and brown in the other) and 4:5 (green and yellow). Following (Koshel *et al.*, 2008; Izrailsky *et al.*, 2008) one can analyze the chaotization evolution when the amplitude of the core oscillation (rotation) increases. On the one hand, with increasing amplitude widths of the resonances also increase, i.e. the extent of overlap grows. On the other hand, the oscillation frequency decreases resulting

in resonances approaching the separatrix, which means that the boundaries (both internal and external) of the chaotization domain approach the separatrix. As a result the mixing is intensified but the chaotic zone does not grow.

Figure 10b represents an example where the amplitude is quite large so that the frequency is slightly less than the maximal rotating frequency in the recirculation zones. The nonlinear resonances 1:1 emerge in the recirculation zones near the elliptic points (see Fig. 9); the resonances are marked by green and orange in one recirculation zone and yellow and brown in the other one. We note that in each recirculation zone two separatrices merge into one separatrix which does not envelop an elliptic point but has a hyperbolic point in the place of elliptic point of the unperturbed recirculation zones. This means that the frequency is almost equal to the maximal rotation frequency at the elliptic point and effects of the resonances are related to its finite width in the frequency (Koshel, *et al.*, 2008). As compared with Figure 10a, the chaotic zone widens slightly in the external flow due to a partial destruction of the resonances 1:2 (blue and dark blue) and in the vicinity of the core due to full destruction of the resonances 1:1; and, more strongly, inside the recirculation zones due to destruction of the fractional resonances (Ryzhov *et al.*, 2010; Koshel *et al.*, 2008; Izrailsky *et al.*, 2008). In this case the chaotic zone approaches very close to the vortex core (the regular domain width here is of order 0.04). Widening of the chaotic zone in the external domain also approaches its maximum: here, with further increasing oscillation amplitude, the zone either remains unchanged (if widening of the resonances compensates the frequency decreasing) or decreases.

Another effect is that with further increasing oscillation amplitude the resonances 1:1 approach the separatrix inside the recirculation zones. When these resonances and the stochastic layer start to overlap, the resonances are partially destroyed with chaotization of the area, including the centers of recirculation zones and the hyperbolic point domain. Figure 10c gives an example of the evolution. With a decrease in the oscillation frequency, the chaotic region slightly decreases. The domains of undestroyed resonances in the recirculation zones are minimal. The Poincare sections clearly show hyperbolic points inside the recirculation zones which is related to the fact that the vicinity of the hyperbolic point is effectively ventilated, i.e., markers do not stay here too long (Budyansky *et al.*, 2004; Kozlov *et al.*, 2005).

Figure 10d shows the rotation motion regime along the phase trajectory far from the elliptic point in Figure 4c. The resonances 1:1 (the same colors as on frames b, c) absorbed by the stochastic sea move away from the centers of the recirculation zones, and each such zone is a rather large domain of regular behavior with central elliptic point (Ryzhov and Koshel, 2010; Koshel *et al.*, 2008; Izrailsky *et al.*, 2008). Small stability islands can be seen in Figure 10d; the positions of the islands corresponding to the frequency rotation equal to 0.768. In the outer region, one can see small patches of undestroyed 1:3 resonances (blue and dark blue).

Figure 11 demonstrates evolution of the Poincare sections in time for the regime of rotation; the time shift is equal to $1/8$ of the period T of core rotation and the marker colors

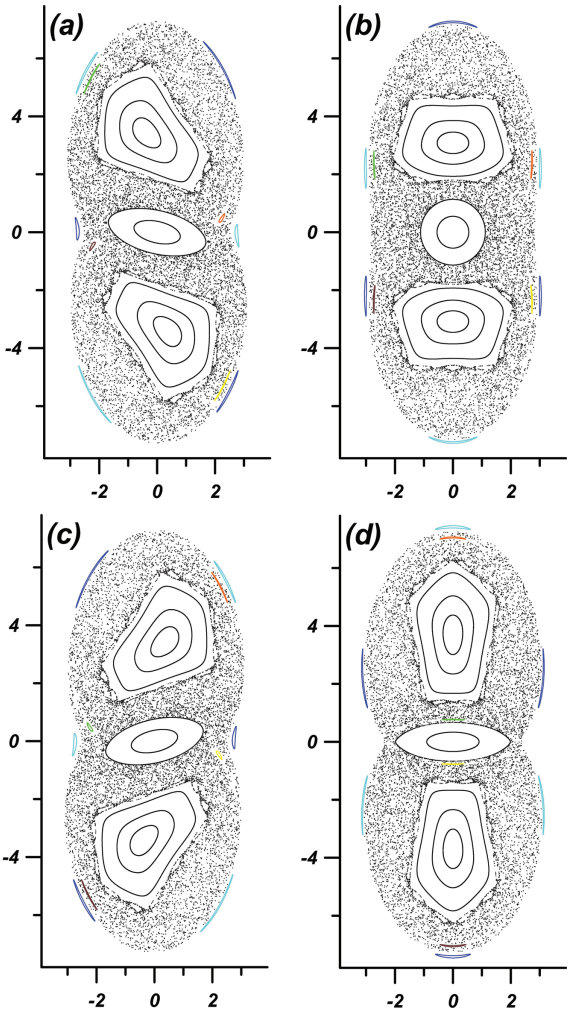

Figure 11. Poincare sections with the parameters corresponding to Figure 10d with a time shift equal to $1/8$ of the period of vortex rotation: (a) $t_n = T/8+nT$; (b) $t_n = T/4+nT$; (c) $t_n = 3T/8+nT$; (d) $t_n = T/2 + nT$.

are as in Figure 10d. Sequence of these sections shows the motion of the characteristic zones during one-half revolution of the vortex core. Figure 10d shows the trajectory positions at the moments nT, and Figure 11a - at the moments $T/8 + nT$. Comparison of Figures 10d and 11 show that the vortex core has an anticyclonic direction of rotation. The fluid in a vicinity of the core also rotates in the same direction. Inside the recirculation zones the fluid rotates about stationary elliptic points in a cyclonic direction (it may be seen by the motion of residual stability islands 1:1). In the external flow the fluid also rotates in a

cyclonic direction about the area that includes the core and the recirculation zones. All particles located in the chaotic zone may perform the motion in any of the three regimes since they may appear in any place of the chaotic sea due to separatrix destruction. Figure 11b corresponds to particle positions at the moments $T/4+nT$, corresponding to the upper boundary of the phase portrait in Figure 4c.

We now give a more precise definition to the phase portraits. Generally speaking, the portraits in Figures 3 and 4 should be considered on a torus which can be constructed in the following way. Since the rotation (or oscillation) frequency of the vortex core is half the frequency of the eccentricity alteration, the phase portrait is a cylinder consisting of four rectangles similar to ones shown in Figures 3 and 4. These rectangles correspond to $-\pi/4 < \theta < \pi/4$ (as in Figs. 3 and 4), $\pi/4 < \theta < 3\pi/4$, $5\pi/4 < \theta < 7\pi/4$, and $3\pi/4 < \theta < 5\pi/4$. All rectangles are connected by the top and bottom boundary, respectively. The first two rectangles are connected with each other by the lines $\theta = -\pi/4$ and $\theta = 3\pi/4$, and the other two, by the lines $\theta = 3\pi/4$ and $\theta = 7\pi/4$. Then the cylinders are linked by the lines. Additionally, it is necessary to append a part of the cylinder for $0 < \varepsilon < 1$ and finally close all the parts to form a torus, so that the ends of the resulting cylinder will be connected when $\varepsilon = 0$, and $\varepsilon = \infty$. Thus, Figure 11b corresponds to the bottom boundary of the rectangle $-3\pi/4 < \theta < -\pi/4$, and the eccentricity reaches its minimal value on this boundary and on the upper boundary of the phase portrait in Figure 4. Since the eccentricity alteration period is half the rotating period of the core, there are nonlinear resonance pairs with the same winding numbers. Figures 11c and 11d show the Poincare sections at the moments $3T/8 + nT$ and $T/2 + nT$, respectively.

Finally, we consider an example of how chaotization depends on the depth. Zhmur and Pankratov (1989) yield estimates showing that the influence of the vortex decays quite rapidly with increasing depth. Figure 12 illustrates the Poincare sections for the case shown in Figure 10c for different depth horizons. One can see in Figure 12 that the chaotization decreases with depth that may be explained by a decrease of amplitude of the nonstationary perturbation, while the perturbation frequency does not depend on the depth. The regular region is minimal in the vicinity of the core slightly below the core boundary. Chaotization effects almost disappear in the horizon $z = 3.0$ (see Fig. 12d). The core has no influence at the level $z = 4.0$; this is in agreement with estimates by Zhmur and Pankratov (1989). Such dynamics is typical for all motion regimes described above. These results confirm the legitimacy of the model of infinitely deep ocean in this case since the core influence does not extend to distances of the order of typical oceanic depth. Fluid mixing is appreciable within a distance equal to the core's vertical semi-axis from the core bottom boundary.

6. Conclusion and discussion

We considered possible regimes of the dynamics of an ellipsoidal vortex embedded into external deformation flow. Special attention was paid to regimes of localized motions of the vortex core: oscillations and rotations. The oscillation regime was shown to lead

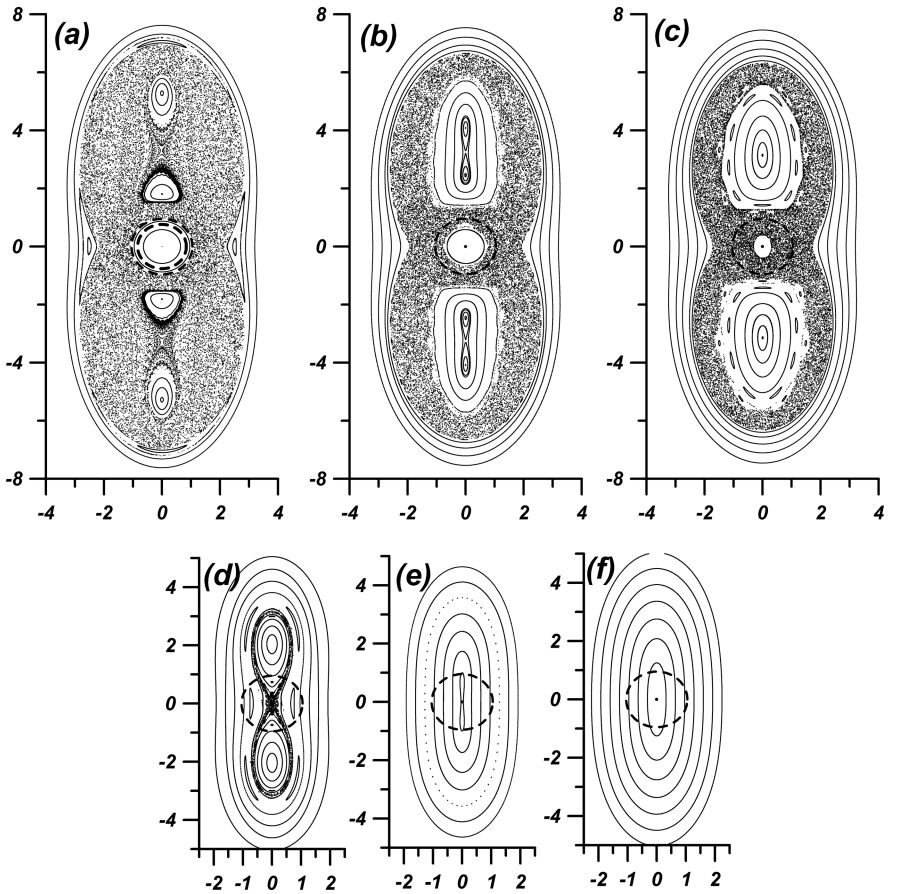

Figure 12. Poincare sections with parameters corresponding to Figure 10d at different horizons of the depths: (a) $z = 0.6$; (b) $z = 1.0$; (c) $z = 1.3$; (d) $z = 3.0$; (e) $z = 3.7$; f) $z = 4.0$.

to chaotization of fluid particle trajectories outside the core. Extent of the chaotization depends on the amplitude of the core oscillation which is taken to be the maximal deviation of eccentricity of the core from its value in stationary state of the vortex. By increasing the amplitude from zero, the chaotization first also increases but next it may decrease. This effect occurs due to the fact that when the amplitude increases, the frequency of oscillation (rotation) decreases. As shown by Izrailsky *et al.* (2006, 2008) and Koshel *et al.* (2008) the finite amplitude boundary of the chaotic zone is determined by overlapping of the widest nonlinear resonances. When the perturbation frequency decreases the resonances approach the separatrices and in doing so they reduce the chaotic zone. Thus, we have an optimal for chaotization amplitude of perturbation instead of the optimal frequency in Izrailsky *et al.* (2006, 2008) and Koshel *et al.* (2008).

Another interesting effect is that the nonlinear resonances appear as pairs due to the double periodicity of core motion. As a result the chaotization becomes stronger since the resonances may overlap not only with resonances of a different order, but also with pair resonances of the same order. Dependence of the chaotization on the depth relative to the vortex center was examined also. The chaotization was shown to be considerable on the depths up to two vertical semi-axes of the ellipsoid and the influence of the vortex disappears practically on the depths exceeding four the semi-axes.

We consider mesoscale and submesoscale eddies; i.e., the perturbations with horizontal scales lying in the range between the ocean depth H and the Rossby deformation radius L_R (Ivanov *et al.*, 1986). Typical values of the buoyancy frequency, Coriolis parameter, and the ocean depth are $\bar{N} = 2 \cdot 10^{-3}\,\mathrm{s}^{-1}$, $f = 10^{-4}\,\mathrm{s}^{-1}$, and $H = 4 \cdot 10^{3}\,\mathrm{m}$, respectively. Therefore we have $L_R = H\bar{N}/f = 8 \cdot 10^{4}\,\mathrm{m}$. Let the horizontal scale be $L = 10\,\mathrm{km}$, the velocity scale be $U = 0.1\,m/c$, in this case the Rossby number is small $R_0 = \frac{U}{fL} = 0.1$. For the same U and f but $L \approx L_R$ it is small too $R_0 \approx 0.01$. We suppose that the dimensionless value of the buoyancy frequency is unity, and the Burger number must be O(1) or less. If $B = \frac{\bar{N}h}{fL} = 1$ for $L = 10\,\mathrm{km}$ we obtain the vertical scale $h = \frac{f}{\bar{N}}L = 0.5\,\mathrm{km}$. For the same $B \approx 1$ and $L \approx L_R$ we have $h = \frac{f}{\bar{N}}L \approx 4\,\mathrm{km}$. If Burger number is small (for example $B \approx 0.1$) but $L \approx L_R$ the vertical scale is $h = \frac{f}{\bar{N}}L = 0.4\,\mathrm{km}$. So suggested theory is valid for mesoscale and submesoscale eddies. Now we can estimate a, b, c. Horizontal semi axes a and b should be chosen in the range $H < L \leq L_R$. Vertical semi axis c may be order from 100 m to 0.5 km.

The investigated model is rough, but it reproduces many characteristic features of saline thermocline lenses (Armi and Zenk, 1984; Armi *et al.*, 1989; Meacham *et al.*, 1994; Filyushkin *et al.*, 2010).

In the absence of viscosity the vortex core boundary is a material surface and fluid particles cannot intersect it (e.g. Brown and Samelson, 1994). However, as we saw, the regular domain in the vicinity of the core boundary can be very narrow. Therefore, diffusion or hydrodynamical instability (Sokolovskiy and Verron, 2000; Sokolovskiy, *et al.*, 2010; Carton, 2009; Dritschel, 2010; Perrot *et al.*, 2010), can result in vorticity emanation from the vortex core. At an initial stage the vorticity may be transported like a passive marker and the structure of chaotic zone can be used as a pattern to study vorticity loss of the vortex core. Such mechanism could be effective in symmetrization of vortices or formation of three-vortex structures (Pingree and Cann, 1992; van Heijst *et al.*, 1991).

Acknowledgments. The paper was supported by the RFBR: project N 11-05-91052-a, FEBRAS: 09-I-П4-01, 11-III-B-07-005.

REFERENCES

Aref, H. 1990. Chaotic advection of fluid particles. Phil. Trans. R. Soc. Lond. A, *333*, 273–288.
—— 2002. The development of chaotic advection. Phys. Fluids, *14*, 1315–1325.

Armi, L., D. Hebert, N. Oakey, J. Price, P. Richardson, T. Rossby and B. Ruddick. 1989. Two years in the life of a Mediterranean salt lens. J. Phys. Oceanogr., *19*, 354–370.

Armi, L. and W. Zenk. 1984. Large lenses of highly saline Mediterranean water. J. Phys. Oceanogr., *14*, 1560–1576.

Arnol'd, V. I. 1989. Mathematical Methods of Classical Mechanics, 2nd ed., Springer, NY, 525 pp.

Bane, J. M., L. M. O'Keefe and D. R. Watts. 1989. Mesoscale eddies and submesoscale coherent vortices: their existence near and interaction with the Gulf Stream, *in* Mesoscale/Synoptic Coherent Structures in Geophysical Turbulence, J. C. J. Nihoul and B. M. Jamart, eds., Elsevier, Amsterdam, 501–518.

Bernstein R. L. 1974. Mesoscale ocean eddies in the North Pacific: Westward propagation. Science, *183*, 71–72.

Brown, M. G. and R. M. Samelson. 1994. Particle motion in vorticity-conserving, two-dimensional incompressible flows. Phys. Fluids, *6*, 2875–2876.

Budyansky, M., M. Uleysky and S. Prants. 2004. Hamiltonian fractals and chaotic scattering by a topographical vortex and an alternating current. Physica D, *195*. 369–378.

Carlson, B. C. and J. L. Gustafson. 1993. Asymptotic approximations for symmetric elliptic integrals. http://arxiv.org/abs/math/9310223v/.

Carton, X. 2009. Instability of surface quasigeostrophic vortices. J. Atmos. Sci., *66*, 1051–1062.

Chaplygin, S. A. 2007. On a pulsating cylindrical vortex. Reg. Chaotic Dyn., *12*, 101–116. (Originally published in: Trudy otdeleniya fizicheskikh nauk Moskovskogo obshchestva lyubitelei estestvoznaniya, Transactions of the Physical Section of Moscow Society of Friends of Natural Sciences, 1899, *10*, 13–22.)

Dahleh, M. D. 1992. Exterior flow of the Kida ellipse. Phys. Fluids A, *4*, 1979–1985.

Danabasoglu, G., J. C. McWilliams and P. R. Gent. 1994. The role of mesoscale tracer transports in the global ocean circulation. Science, *264*, 1123–1126.

del-Castillo-Negrete, D. and P. J. Morrison. 1993. Chaotic transport by Rossby waves in shear flow. Phys. Fluids A, *5*, 948–965.

Dritschel., D. G. 2010. An exact steadily rotating surface quasi-geostrophic elliptical vortex. Geophys. Astro. Fluid Dyn., *105*, 368–376.

Dritschel, D. G., J. N. Reinaud and W. J. McKiver. 2004. The quasi-geostrophic ellipsoidal vortex model. J. Fluid Mech., *505*, 201–223.

Fedorov, K. N. and A. I. Ginzburg. 1986. "Mushroom-like" currents (vortex dipoles) in the ocean and in a laboratory tank. Ann. Geophys., *4*, 507–516.

Filyushkin, B. N., M. A. Sokolovskiy, N. G. Kozhelupova and I. M. Vagina. 2010. Dynamics of intrathermocline lenses. Doklady Earth Sci., *434*, 1377–1380.

Gudimenko, A. I. 2007. Chaos and resonances in a rotating flow disturbed by a periodic motion of a point vortex. Russian Sci. J. Nonlinear Dyn., *3*, 33–48.

Holland, W. R. 1978. The role of mesoscale eddies in the general circulation of the ocean: Numerical experiments using a wind-driven quasigeostrophic model. J. Phys. Oceanogr., *8*, 363–392.

Ivanov, Iu. A., V. G. Kort, A. S. Monin, I. M. Ovchinnikov and I. F. Shadrin. 1986. Mesoscale inhomogeneities of the ocean. Akademiia Nauk SSSR, Doklady, *289*, 706–709.

Izrailsky, Yu. G., K. V. Koshel and D. V. Stepanov. 2006. Determining the optimal frequency of perturbation the problem of chaotic transport of particles. Dokl. Phys., *51*, 219–222.

—— 2008. Determination of optimal excitation frequency range in background flows. Chaos, *18*, 013107, doi:10.1063/1.2835349.

Kawakami, A. and M. Funakoshi. 1999. Chaos motion of fluid particles around a rotating elliptic vortex in a linear shear flow. Fluid Dyn. Res., *25*, 167–193.

Kida, S. 1981. Motion of an elliptic vortex in a uniform shear flow. J. Phys. Soc. Jpn., *50*, 3517–3520.

Koshel, K. V. and S. V. Prants. 2006. Chaotic advection in the ocean. Physics – Uspekhi, *49*, 1151–1178.

Koshel, K. V., M. A. Sokolovskiy and P. A. Davies. 2008. Chaotic advection and nonlinear resonances in an oceanic flow above submerged obstacle. Fluid Dyn. Res., *40*, 695–736.

Kozlov, V. F. and K. V. Koshel. 1999. Barotropic model of chaotic advection in background flows. Izvestia, Atmos. Oceanic Phys., *35*, 123–130.

—— 2000. A model of chaotic transport in the barotropic background flow. Izvestia, Atmos. Oceanic Phys., *36*, 109–118.

Kozlov, V. F., K. V. Koshel and D. V. Stepanov. 2005. Influence of the boundary on chaotic advection in the simplest model of a topographic vortex. Izvestia, Atmos. Oceanic Phys., *41*, 217–227.

McWilliams, J. C. 1976. Maps from the Mid-Ocean Dynamics Experiment: Part I. Geostrophic stream-function. J. Phys. Oceanogr., *6*, 810–827.

—— 1985. Submesoscale, coherent vortices in the ocean. Rev. Geophys., *23*, 165–182.

Meacham S. P. 1992. Quasigeostrophic, ellipsoidal vortices in stratified fluid. Dyn. Atmos. Oceans, *16*, 189–223.

Meacham, S. P., G. R. Flierl and U. Send. 1989. Vortices in shear. Dyn. Atmos. Oceans, *14*, 333–386.

Meacham, S. P., K. K. Pankratov, A. F. Shchepetkin and V. V. Zhmur. 1994. The interaction of ellipsoidal vortices with background shear flows in a stratified fluid. Dyn. Atmos. Oceans, *21*, 167–212.

Meleshko, V. V. and H. Aref. 1996. A blinking rotlet model for chaotic advection. Phys. Fluids., *8*. 3215–3217.

Monin, A. S., V. M. Kamenkovich and V. G. Kort. 1977. Variability of the Oceans. (English tanslation edited by J. L. Lumley - translated from Russian. Originally published by Hydrometeoisdat, 1974), Wiley, NY, 241 pp.

Muyazaki T., Y. Furuichi and N. Takahashi. 2001. Quasigeostrophic ellipsoidal vortex model. J. Phys. Soc. Japan, *70*. 1942–1953.

Muyazaki, T., K. Ueno and T. Shimonishi. 1999. Quasigeostrophic tilted spheroidal vortices. J. Phys. Soc. Japan, *68*, 2592–2601.

Pankratov, K. K. and V. V. Zhmur. 1991. A dynamics of desinglarized quasigeostrophic vortices. Physics of Fluids A, Fluid Dynamics, *3*, p. 1464.

Pedlosky, J. 1987. Geophysical Fluid Dynamics, 2nd ed., Springer, NY, 710 pp.

Perrot, X., J. N. Reinaud, X. Carton and D. G. Dritschel. 2010. Homostrophic vortex interaction under external strain, in a coupled QG-SQG model. Regul. Chaotic Dyn., *15*, 66–83.

Pingree, R. D. and B. Le Cann. 1992. Anticyclonic Eddy X91 in the Southern Bay of Biscay, May 1991 to February 1992. J. Geophys. Res., *97*, 14353–14367.

Polvani, L. M. and J. Wisdom. 1990. Chaotic Lagrangian trajectories around an elliptical vortex parch embedded in a constant and uniform background shear flow. Phys. Fluids A, *2*, 123–126.

Prants, S. V., M. V. Budyansky, M. Yu. Uleysky and G. M. Zaslavsky. 2006. Chaotic mixing and transport in a meandering jet flow. Chaos, *16*, 033117, doi:10.1063/1.2229263.

Reznik G. M. 1992. Dynamics of singular vortices on a beta-plane. J. Fluid Mech., *240*, 405–432.

Rom-Kedar, V., A. Leonard and A. Wiggins. 1990. Analytical study of transport, mixing and chaos in unsteady vortical flow. J. Fluid Mech., *214*, 347–394.

Ryzhov, E. A. and K. V. Koshel. 2010. Chaotic transport and mixing of a passive admixture by vortex flows behind obstacles. Izvestia, Atmos. Oceanic Phys., *46*, 184–191.

Ryzhov, E. A., K. V. Koshel and D. V. Stepanov. 2010. Background current concept and chaotic advection in an oceanic vortex flow. Theor. Comput. Fluid Dyn., *24*, 59–64.

Shariff, K., A. Leonard and J. H. Ferziger. 2006. Dynamical systems analysis of fluid transport in time-periodic vortex ring flows. Phys. Fluids, *18*, 047104, doi:10.1063/1.2189867.

Sokolovskiy, M. A. and J. Verron. 2000. Finite-core hetons: Stability and interactions. J. Fluid Mech., *423*, 127–154.

Sokolovskiy, M., J. Verron, X. Carton and V. Gryanik. 2010. On instability of elliptical hetons. Theor. Comput. Fluid Dyn., *24*, 117–123.

Thomson, W. 1867. On vortex atoms. Phil. Mag. Ser. 4, *34*, 15–24.

van Heijst, G. J. F., R. C. Kloosterziel and C. W. M. Williams. 1991. Formation of a tripolar vortex in a rotating fluid. Phys. Fluids A, *3*, 2033.

Wiggins, S. 1990. Introduction to Applied Nonlinear Dynamical Systems and Chaos, Springer, NY, 688 pp.

Zaslavsky, G. M. 2007. Physics of Chaos in Hamiltonian Systems, Imperial College Press, London, 328 pp.

Zhmur, V. V. 1989. Subsurface mesoscale eddy structures in a stratificated ocean. Oceanology, *29*, 28–32.

—— 1988a. Localized eddy formation in a shear-flow. Oceanology, *28*, 536–538.

—— 1988b. Disk model of mesoscale eddy in shear-flow. Oceanology, *28*, 709–714.

Zhmur, V. V. and K. K. Pankratov. 1989. Dynamics of a semi-ellipsoidal subsurface vortex in a nonuniform flow. Oceanology, *29*, 205–211.

—— 1990a. Dynamics of submesoscale eddy in a flow field of a large strong vortex. Oceanology, *30*, 170–178.

—— 1990b. Steady quasigeostrophic vortices with a nonuniform potential vorticity of the core. Oceanology, *30*, 378–386.

Zhmur, V. V. and A. F. Shchepetkin. 1991. Evolution of an ellipsoidal vortex in a stratified ocean. Survivability of the vortex in a flow with vertical shear. Izv. Atmos. Oceanic Phys., *27*, 492–503.

—— 1992. The interaction of 2 quasigeostrophical baroclinic vortices – the tendency to come together and merge. Izv. Atmos. Oceanic Phys., *28*, 538–551.

Received: *1 January, 2011*; revised: *5 May, 2011*.